

Size and Temperature Effects on the Fracture Mechanisms of Silicon Nanowires: Molecular Dynamics Simulations

Keonwook Kang, Wei Cai

Department of Mechanical Engineering, Stanford University, CA 94305-4040

Abstract

We present molecular dynamics simulations of $[1\ 1\ 0]$ -oriented Si nanowires (NWs) under a constant strain rate in tension until failure, using the modified embedded-atom-method (MEAM) potential. The fracture behavior of the NWs depends both on temperature and NW diameter. For NWs of diameter larger than 4 nm, cleavage fracture on the transverse $(1\ 1\ 0)$ plane are predominantly observed at temperatures below 1000 K. At higher temperatures, the same NWs shear extensively on inclined $\{1\ 1\ 1\}$ planes prior to fracture, analogous to the brittle-to-ductile transition (BDT) in bulk Si. Surprisingly, NWs with diameter less than 4 nm fail by shear regardless of temperature. Detailed analysis reveals that cleavage fracture is initiated by the nucleation of a crack, while shear failure is initiated by the nucleation of a dislocation, both from the surface. While dislocation mobility is believed to be the controlling factor of BDT in bulk Si, our analysis showed that the change of failure mechanism in Si NWs with decreasing diameters is nucleation controlled. Our results are compared with a recent *in situ* tensile experiment of Si NWs showing ductile failure at room temperature.

Keywords: Fracture mechanisms, Dislocations, Molecular Dynamics

Email addresses: kwkang@stanford.edu (Keonwook Kang), caiwei@stanford.edu (Wei Cai)

1. Introduction

Semiconducting nanowires (NWs) are key building blocks in nanotechnology, with many potential applications such as nano-scale transistors (Cui et al., 2003; Wang et al., 2003; Huang and Lieber, 2004), sensors (Cui et al., 2001b; Hahm and Lieber, 2004; Patolsky et al., 2006), actuators (Chau et al., 2003), power sources (Tian et al., 2007) and battery anodes (Chan et al., 2007). The reliability and manufacturability of these nano-devices depends on the mechanical properties of semiconducting NWs, which, due to their small sizes, are expected to be different from bulk semiconductors. NWs also provide a useful test-bed to compare experiments and theoretical models on the deformation behavior of materials at the nano-scale. Such comparisons are important to deepen our understanding on the dynamics of crystal defects such as dislocations and cracks, which control not only the deformation behavior of nano-sized materials but also that of bulk materials.

The mechanical properties of semiconducting NWs have been measured both in tensile tests (Kizuka et al., 2005; Han et al., 2007) and in bending tests (Paulo et al., 2005; Heidelberg et al., 2006; Hoffmann et al., 2006). At the same time, through the use of parallel computers, Molecular Dynamics (MD) simulations are able to handle millions of atoms at an acceptable speed so that reasonably sized NWs can be directly modelled. Therefore experimental tests and MD simulations of NW deformation can be compared on the same length scale, even though there is still a significant challenge in comparing the two at the same time scale.

Various methods have been used to grow single crystal silicon NWs (Morales and Lieber, 1998; Holmes et al., 2000; Cui et al., 2001a; Ma et al., 2003; Wu et al., 2004). The range of diameters and the preferred orientation of the NWs depend on the growth method and experimental condition. Using chemical vapor deposition (CVD), Si NWs with diameters ranging from 3 to 30 nm have been obtained, and the NWs prefer to grow along the $[1\ 1\ 0]$ direction if their diameters are less than 10 nm (Cui et al., 2001a; Wu et al., 2004). Si NWs as thin as 1.3 nm in diameter can be obtained using the oxide assisted growth method (Ma et al., 2003).

Here we present MD simulation results on tensile tests of $[1\ 1\ 0]$ -oriented Si NWs with diameters ranging from 2 nm to 7 nm, under the temperature range from 100 K to 1200 K. We observe that, NWs with large diameters fail by cleavage fracture on the transverse $(1\ 1\ 0)$ plane at low temperatures. At elevated temperatures, the same NWs shear extensively on inclined $\{1\ 1\ 1\}$

planes prior to fracture. This is analogous to the brittle-to-ductile transition (BDT) of bulk Si. More interestingly, Si NWs with diameters less than 4 nm fail by shear regardless of temperature. This is analogous to the recent report of ductile fracture of [1 1 0]-oriented Si NWs at room temperature in *in situ* tensile experiments (Han et al., 2007). On the other hand, this size effect is not observed in [1 1 1]-oriented Si NWs, which show cleavage fracture at room temperature even down to $D = 2$ nm. This is consistent with recent tensile experiments of Zhu et al. (2009).

The paper is organized as follows. Section 2 describes the simulation method. Section 3 presents the simulation results, including the fracture strength and the dependence of fracture mechanism on temperature and NW diameter. Detailed analysis of the first nucleation event that leads to cleavage and shear failure are also presented. Section 4 presents the arguments for a nucleation-based model that may explain the size dependence of the fracture mechanisms, and compares it against the dislocation-mobility based BDT model for bulk Si. A brief summary is given in Section 5.

2. Methods

2.1. Interatomic potential model

It is known that many interatomic potential models for Si incorrectly predict ductile fracture of bulk Si at room temperature. (Hauch et al., 1999) The suitability of potential models for studying fracture mechanisms in Si and Ge NWs was the focus of our earlier paper (Kang and Cai, 2007). We found that the MEAM potential (Baskes, 1992; Baskes et al., 1994; Baskes, 1997, 1999) is the most reliable among all the models we had tested for the study of fracture in Si. This is because the ratio between the ideal tensile strength and the ideal shear strength of the bulk determines to a large extent the brittle versus ductile behavior of the model, and the ratio predicted by the MEAM model is the closest to *ab initio* predictions. In this work, We further tested the accuracy of the MEAM potential in describing the surface reconstruction of Si NWs by comparing with *ab initio* results (Appendix A). The Si MEAM potential parameters we used are listed in Table A.1, and other properties such as surface energy and surface stress are listed in Tables A.3 and A.4. Because the MEAM potential is computationally more expensive than other models, such as Stillinger and Weber (1985) and Tersoff (1989), we applied a set of measures to enhance numerical efficiency, as described in the following section.

2.2. Simulation setup

The NWs are prepared by first creating a perfect diamond-cubic crystal of Si with lattice constant $a = 5.431\text{\AA}$ and then removing all atoms outside a cylindrical region of a specified diameter D . In this manner, NWs in the simulations have a nominally circular cross section, so that no length scale other than the diameter needs to be considered. This has the advantage of reducing the parameter space of study compared with studying NWs with faceted cross section.¹ The atomic structures are then relaxed by the conjugate gradient algorithm to a local energy minimum, with the NW length kept constant. In our model, the NW surface is exposed to vacuum, *i.e.*, neither an oxide nor a hydrogen passivation layer is considered. The main reason for studying bare NW is to avoid the complexities in the reliability of silicon-oxygen or silicon-hydrogen interatomic potentials on their mechanical properties predictions. We also hope that, if there exists a fundamental size effect on the fracture mechanisms in real Si NWs, it should also appear in a bare Si NW model. The cross-sections of the relaxed NWs are shown in Fig. 1 and their dimensions are given in Table 1. The aspect ratio (diameter D : length L_z) of all NWs is around 1 : 10. Periodic boundary conditions (PBC) are applied along the NW axis. The relaxed structures are used as initial conditions for subsequent MD simulations.

In general, the simulation procedure for the tensile deformation is similar to that used in our previous work (Kang and Cai, 2007), except for the following modifications to enhance numerical efficiency. For time integration in MD, we use the Liouville-type velocity Verlet integrator (Martyna et al., 1996), which is a symplectic integrator and allows us to use a larger time

¹Small facets naturally appear due to discreteness of the lattice, even in the nominally circular cross sections as shown in Fig. 1.

	D (nm)	\mathbf{e}_z	L_z (nm)	N_{tot}
Table 1: Diameter D , PBC repeat vector \mathbf{e}_z , NW length L_z and total number of atoms N_{tot} for the NWs in this study. The aspect ratio $D : L_z$ is kept at approximately 1:10 for all NWs.	2	$25 \times [110]$	19.2	3100
	3	$40 \times [110]$	30.7	10400
	4	$52 \times [110]$	39.9	25584
	5	$65 \times [110]$	49.9	47580
	6	$78 \times [110]$	59.9	84552
	7	$91 \times [110]$	69.9	133224

step of 1 fs (compared to 0.1 fs in Kang and Cai (2007)). The MD simulations are performed using the LAMMPS program (Plimpton, 1995) with multiple CPUs. Before loading the NWs in tension, we equilibrate them for 20 ps in the NPT ensemble at the specified temperature and zero axial stress. This removes any axial stress (σ_{zz}) that can develop due to thermal expansion or surface reconstruction. The stress inside the NWs is calculated using the Virial formula (Chueng, 1977; Marc and McMillan, 1985; Cormier et al., 2001b,a; Dommelen, 2003).² After equilibration, the tensile simulations are performed using the NVT ensemble, in which the NWs are elongated by 0.01% of the initial length at every 0.2 ps until it breaks. This corresponds to a strain rate of $5 \times 10^8 \text{ s}^{-1}$, which is a factor of 10 smaller than that in Kang and Cai (2007). The choice of high strain rate of $5 \times 10^8 \text{ s}^{-1}$ is ultimately determined by the limited computing resources, especially because we need to sample a wide range of temperature and diameters. The instantaneous Virial stress is averaged over each 0.2 ps period. The temperature is controlled by the Nosé–Hoover thermostat (Nosé, 1984; Hoover, 1985) with the “thermal mass” parameter set such that the characteristic time for temperature fluctuation is $\tau = 10$ fs in all simulations. When NW fracture is observed, we re-run the simulation for another 10 times, starting from the moment that is 20 ps before the onset of fracture. At the beginning of these repeated simulations, the atomic velocities are randomized following the Gaussian distribution corresponding to the specified temperature. The purpose of these simulations is to assess the repeatability of the observed fracture behavior.

All the tensile simulations in this paper are performed at strain rate of $\dot{\epsilon} = 5 \times 10^8 \text{ s}^{-1}$ for [1 1 0]-oriented Si NWs, unless otherwise specified. In a few cases, we employed strain rate of $\dot{\epsilon} = 5 \times 10^7 \text{ s}^{-1}$, elongating NWs by 0.01% of the initial length at every 2 ps, to test the strain rate effect. We

²The Virial stress is computed as a sum over all atoms (and atom pairs) in the simulation cell and divided by the cell volume, which is the NW length L_z times the cross section area A in this work. Therefore, the magnitude of the Virial stress depends on our definition of the NW cross section area. Here we compute the area by $A = \pi D^2/4$, where D is the nominal diameter. When the NW is first created, all atoms outside the cylinder of diameter D is removed. Due to the discreteness of atomic positions, one may argue that the “real” diameter of the NW should be somewhat smaller than D . This discrepancy becomes larger for thinner NWs as reported by Gall et al. (2004) and Wu et al. (2005). For the thinnest NW ($D = 2$ nm), the “real” area may be 10% smaller and the “real” stress may be 10% higher than the values reported here.

also simulated a few $[1\ 1\ 1]$ -oriented Si NWs at room temperature to test the orientation effect.

3. Results

3.1. Stress-strain relation

Fig. 2(a) presents the stress-strain curves for Si NW of $D = 5$ nm at different temperatures, showing temperature effect on fracture strength. As temperature increases from 300 K to 1200 K, the fracture strength monotonically decreases from 12.8 GPa to 5.2 GPa. The slope of the stress-strain curve near zero strain gives the Young's modulus, $E_{[110]}$, which also decreases at higher temperatures. This softening behavior is observed for NWs of all sizes in this study. Fig. 2(b) shows the stress-strain curve for NWs with different diameters at $T = 300$ K, exhibiting a size effect. While the stress-strain curves of NWs with $D > 4$ nm almost overlap with each other, NWs with $D = 2$ nm and $D = 3$ nm show a significant reduction in both Young's modulus and fracture strength. This size effect persists, even if we take into account of the possibility that the stress in the thinnest NWs may have been underestimated by 10% due to the uncertainties in defining the NWs cross section area.

In Fig. 3(a), tensile stress-strain curves of a $[1\ 1\ 0]$ Si NW of $D = 5$ nm are plotted in the range of strain rate from 5×10^7 s $^{-1}$ to 5×10^9 s $^{-1}$. The data at $\dot{\epsilon} = 5 \times 10^9$ s $^{-1}$ is taken from Kang and Cai (2007). The stress-strain curves at these strain rates overlap with each other until the NW breaks. However, the fracture strength was found to reduce from 13.2 GPa to 12.1 GPa, as the strain rate decreases. This is because defects can nucleate at lower stresses if it is given more time. Fig. 3(b) shows stress-strain curves of Si NWs of $D = 5$ nm with $[1\ 1\ 1]$ and $[1\ 1\ 0]$ orientations. The fracture strength is 15.3 GPa for the $[1\ 1\ 1]$ NW, and 12.8 GPa for the $[1\ 1\ 0]$ NW. In the entire diameter range ($D = 2 \sim 7$ nm) and at room temperature, we observed that the fracture strength of the $[1\ 1\ 0]$ NW is always lower than that of the $[1\ 1\ 1]$ NW with the same (nominal) diameter.

Fig. 4(a) plots the Young's modulus of Si NWs as a function of NW diameter at $T = 300$ K. The Young's modulus of $[1\ 1\ 0]$ - and $[1\ 1\ 1]$ -oriented Si NWs are obtained by fitting the stress-strain curve to a straight line in the strain range of 0 to 1%. For comparison, 1% Young's moduli along $\langle 1\ 1\ 0 \rangle$ and $\langle 1\ 1\ 1 \rangle$ directions in bulk Si are computed at room temperature

and drawn as two horizontal lines in Fig. 4(a). First, the Young's modulus of [1 1 0]-oriented Si NWs is always lower than that of [1 1 1]-oriented Si NWs with the same diameter in the range of $D = 2$ to 7 nm. Second, the Young's modulus decreases as the diameter decreases, regardless of NW orientation. The Young's modulus of the [1 1 0] NW of $D = 2$ nm is reduced by 28% from the bulk value (154 GPa at 300 K for the MEAM model). Similarly, the Young's modulus of the [1 1 1] NW of $D = 2$ nm is reduced by 33% from the bulk value (168 GPa at 300 K for the MEAM model). Lee and Rudd (2007) calculated the Young's modulus of [0 0 1]-oriented NWs by first-principle density functional theory. They also reported a monotonic reduction of Young's modulus as NW diameter decreases. The Young's modulus of a [0 0 1]-oriented NW with $D = 2$ nm is about 26% smaller than the bulk value (122.5 GPa). Even though the NWs in Lee and Rudd (2007) have a different orientation from the NWs in this study, the consistency in the general trend in the size dependence is encouraging. It suggests that a common mechanism is responsible for the reduction of the Young's modulus for Si NWs with different orientations. A similar softening behavior of Young's modulus is observed in the experiments, but the size effect is much more pronounced (Li et al., 2003; Zhu et al., 2009). Li et al. (2003) estimated the Young's modulus to be 53 GPa for $\langle 110 \rangle$ Si cantilevers of thickness 12 nm, by measuring the resonant frequency. Zhu et al. (2009) performed tensile experiments of Si NWs of $D = 15 \sim 60$ nm, and reported Young's modulus to be slightly above 120 GPa for $D = 20$ nm. Though the experiment results support the qualitative trend of Young's modulus reduction as NW size decreases, a quantitative difference still exists between experimental and simulation results. More studies are needed to resolve this discrepancy.

Fig. 4(b) shows the relationship between fracture strength and temperature for all NW diameters ($D = 2 \sim 7$ nm). Each data point is obtained from the average of 10 MD simulations under identical conditions but with different initial velocities. The error bar represents the magnitude of fluctuations of the instantaneous Virial stress, which is in between ± 60 MPa and ± 500 MPa depending on NW diameter and temperature. The curves for $D \geq 4$ nm are close to each other. The strengths of NWs with $D = 2$ nm and $D = 3$ nm are significantly lower than those of thicker NWs in the entire range of temperature.

3.2. Cleavage vs. shear failure

The Si NWs in our MD simulations fail by cleavage fracture on the transverse (110) plane, or by shear on inclined $\{111\}$ planes, or a combination of both, depending on temperature and NW diameter. For example, a typical cleavage fracture is shown in Fig. 5(a)-(d) for a NW with $D = 7$ nm at $T = 300$ K. A crack is nucleated at the NW surface and then cuts through the NW on the (110) plane perpendicular to the NW axis. A typical shear failure is shown in Fig. 5(e)-(h) for the same NW at $T = 1000$ K. In this case, extensive sliding on a $\{111\}$ plane (tilted with respect to the NW axis) is observed, which leads to significant local thinning of the NW before fracture.

There are obvious analogies between this transition of fracture mechanisms with increasing temperature and the brittle-to-ductile transition (BDT) in bulk Si. For brevity, we shall call NW fracture with the cleavage mechanism “brittle” fracture, and NW fracture with shear mechanism “ductile” fracture. However, we emphasize that there is an important difference between the terms “brittle/ductile” used here for Si NWs and the conventional criterion for distinguishing brittle and ductile fracture in bulk materials.

When a bulk material fails by ductile fracture, it consumes significantly more energy than that in the case of brittle fracture. This is because the bulk material undergoes macroscopic yielding (e.g. dislocation induced shear) when it is ductile, whereas the deformation is localized to the crack tip when the material is brittle. However, in our MD simulations, even when the NW fails by dislocation induced shear (a mechanism for ductile fracture), the deformation is still localized in a short section of the NW and does not lead to large energy consumption. In fact, the energy consumption (i.e. the area under the stress-strain curve) decreases with increasing temperature because the NWs break at lower stresses at higher temperatures, as shown in Fig. 2(a). This behavior can be attributed to the small cross section of the NWs, which prevents large-scale yielding even in “ductile” failure.

The failure mechanisms are also influenced by the NW diameter, and NWs of diameter $D = 2$ nm and 3 nm experiences ductile fracture regardless of temperature. For example, snapshots for NWs with $D = 2$ nm are plotted in Fig. 6, showing significant slip and necking even at $T = 100$ K. This is in contrast with NWs with large diameters (e.g. $D = 7$ nm), which exhibit brittle fracture at low temperature, as shown in Fig. 5(a)-(d). Therefore, it is reasonable to expect a transition to occur for NWs with intermediate diameters. Indeed, for NWs with $D = 4$ nm, we observe a fracture behavior different from both limits described above. At $D = 4$ nm, the NW fracture

behavior exhibits larger statistical fluctuation. Specifically, we can observe either brittle or ductile behavior by repeating the MD simulations under identical temperature and loading conditions but different (random) initial velocities. This statistical fluctuation is also observed to some degree in thinner or thicker NWs, but is most pronounced for NWs with $D = 4$ nm.

Fig. 8 summarizes the observed fracture behaviors of Si NWs in the parameter space of NW diameter and temperature. Each symbol shows the fracture behavior of Si NWs from ten independent simulations with random initial velocities. A circle indicates ductile fracture and a cross indicates brittle fracture. A triangle means that, out of the ten simulations, both brittle and ductile behavior have been observed. We can clearly see the size and temperature dependence of fracture behavior in this map. To investigate strain rate effect on the fracture behaviors, we tested Si NWs of $D = 3 \sim 5$ nm at a strain rate of $5 \times 10^7 \text{ s}^{-1}$ at room temperature. The fracture mechanism still changes from ductile mode to brittle mode at $D = 4$ nm.

Interestingly, the size dependence of fracture mechanisms was not observed in the $[1\ 1\ 1]$ -oriented Si NWs in the same diameter range under identical loading conditions at room temperature. The $[1\ 1\ 1]$ NWs fail by cleavage fracture for all test diameters. For example, Fig. 7 shows the cleavage fracture of $[1\ 1\ 1]$ NW of $D = 2$ nm.

In our previous paper (Kang and Cai, 2007), we predicted that a $[1\ 1\ 1]$ -oriented Si NW is more brittle than a $[1\ 1\ 0]$ -oriented Si NW on the ground that the ratio of ideal tensile strength over shear strength multiplied by corresponding Schmid factor is much smaller along the $[1\ 1\ 1]$ direction. The prediction is confirmed here in that the NW in Fig. 7 fails by cleavage fracture while the NW in Fig. 6 fails by shear fracture. The size and orientation dependence of fracture behavior seems to be a unique feature of semiconductor NWs. For metal nanowires (Ni, Au, Cu), there have been several atomistic tension simulations (Ikeda et al., 1999; Branício and Rino, 2000; Gall et al., 2004; Park and Zimmerman, 2006; Park et al., 2006), according to which ductile failures after large deformation are commonly reported regardless of NW size and orientation. The origin of the size dependent failure behavior of Si NWs will be discussed in Section 4.3.

3.3. Slip analysis

In this section, we investigate whether the shear failure of Si NWs is initiated by the nucleation of a dislocation. To detect and characterize a

dislocation, we start by identifying a slip plane and the direction and magnitude of the slip. For this purpose, we define a displacement difference vector which carries the information of how an atomic bond is deformed, as explained below.

Consider a NW structure of length L_z and consisting of N atoms, where atomic positions are specified by $\{\mathbf{x}^i\}$ for $i = 1, 2, \dots, N$. We first construct a reference configuration $\{\mathbf{x}_0^i\}$, by uniformly elongating the initially relaxed NW structure (at zero strain, see Section 2.2.) to the same length L_z . By construction, the reference structure does not contain dislocations but experience the same total strain as the NW structure being analyzed.

The displacement vector of atom i with respect to the reference structure is defined as

$$\mathbf{u}^i \equiv \mathbf{x}^i - \mathbf{x}_0^i \quad (1)$$

and the displacement difference between two atoms i and j is defined as

$$\Delta\mathbf{u}^{ij} \equiv \mathbf{u}^j - \mathbf{u}^i, \quad (2)$$

where i and j are indices of a pair of atoms that formed a bond in the reference configuration. We compute the $\Delta\mathbf{u}^{ij}$ vectors for all atom pairs i and j that are nearest neighbors in the reference configuration. Fig. 9(a) shows that, if a slip plane cuts through the bond between atoms i and j , the $\Delta\mathbf{u}^{ij}$ vector corresponds to the slip vector, which lies on the slip plane. Zimmerman et al. (2001) developed a similar expression for the slip vector, which is Eq. (2) averaged over the nearest neighbors of atom i .

In Fig. 10(a), we examine a simulation snapshot of a Si NW with $D = 4$ nm subjected to tension at room temperature. A line segment is drawn for each atomic bond i - j if the displacement difference vector satisfies the condition

$$|\Delta\mathbf{u}^{ij}| > d_c$$

In this work, we set d_c to be the magnitude of the Burgers vector, $b = 3.84$ Å. Most of the line segments clearly intersects a single plane, which is a shuffle-set $(11\bar{1})$ plane in this case.

Fig. 10(b)–(e) show the displacement difference vectors for all the atomic bonds cut by the identified slip plane. Each vector is projected onto the slip plane, and is placed at the center of the corresponding atomic bond, marked as a dot, in the reference configuration. The dislocation is identified as the boundary between slipped and unslipped areas, and is observed to nucleate

from the surface (at the upper right corner) and sweep through the $(11\bar{1})$ plane. The Burgers vector of the dislocation is identified as $\mathbf{b} = [011]/2$. In Fig. 10(d), the dislocation line becomes nearly straight and takes the pure screw orientation.

Because the NW is subjected to a constant strain rate, we can estimate the critical stress for dislocation nucleation from the time of the nucleation. From Fig. 2(b), we can find that the applied stress σ_{zz} has reached the fracture strength of 13 GPa at $t = 349.4$ ps. The resolved shear stress on this slip system can be obtained by multiplying the Schmid factor $S = 0.4082$, which gives $\tau = S\sigma_{zz} = 5.3$ GPa. It is important to note that τ is much larger than the Peierls stress of a shuffle-set dislocation, which is 2.23 GPa (Appendix A). Therefore, the dislocation will have no difficulty in travelling across the NW once it is nucleated.

At high temperatures (e.g. above 1000 K), thermal fluctuation prevents us from getting a clear picture of dislocation nucleation. However, it seems that at higher temperatures, surface diffusion is quite active and dislocations tend to nucleate at multiple locations and on multiple planes simultaneously. Sometimes multiple slip planes intersect each other, leading to a more complicated fracture behavior. We have also performed the same slip analysis for very thin NWs at low temperatures where shear failure is observed. From these analyses, we conclude that all shear failure observed in our simulations initiates from dislocation nucleation at the surface.

3.4. Crack analysis

We have also applied the displacement difference vector analysis to NWs that ultimately fail by cleavage fracture. The goal is to see whether the initial event is the nucleation of a crack, or perhaps, the nucleation of a dislocation. Fig. 9(b) shows that, if a crack cut through the bond between atoms i and j , the $\Delta\mathbf{u}^{ij}$ vector corresponds to the crack opening displacement, which is perpendicular to the crack plane for a Mode I crack.

In Fig. 11(a), we examine a Si NW with $D = 6$ nm at room temperature. Every bond with $|\Delta\mathbf{u}^{ij}| > 3.84$ Å are plotted in Fig. 11(a). They clearly populate the (110) plane perpendicular to the NW axis, as opposed to a tilted $\{111\}$ plane. Fig. 11(b) shows that the $\Delta\mathbf{u}^{ij}$ vectors are mostly perpendicular to the (110) plane, corresponding to a crack. In Fig. 11(c)–(h), the z component of $\Delta\mathbf{u}^{ij}$ for every bond cut by the (110) plane are plotted in gray scale to show the nucleation and growth of the crack with time. From the snapshots, we can calculate the crack front speed, which is roughly 2 km/s.

This is comparable to the maximum crack speed of 2.59 ± 0.27 km/s on the (1 1 1) plane in the MD fracture simulations of Si beam in Swadener et al. (2002).

This analysis shows that it is indeed the nucleation of a crack that initiates the cleavage fracture of the Si NW. It is interesting to notice that, even though a crack nucleates from the surface, it propagates faster in the interior than on the surface. As a result, the NW structures may look deceptively similar at the beginning of both ductile and brittle failures, if we only examine the NW surface. In both cases a small dent can be observed, as in Fig. 5(a) and Fig. 5(e). However, detailed analysis revealed that two different events have occurred. For ductile failure, it was the nucleation of a dislocation. For brittle failure, it was the nucleation of a crack.

4. Discussion

4.1. Comparison with fracture strength measurements

Our simulations predict that the room temperature fracture strength of thick NWs ($D > 4$ nm) is around 13 GPa along the [1 1 0] direction and 15 GPa along the [1 1 1] direction at the strain rate of 5×10^8 s⁻¹. Due to the difficulty in holding a nanoscale sample and accurately measuring the applied force and the resulting deformation, nano-scale tensile tests are very challenging, and few reliable data on fracture strength are available directly from NW tensile tests. However, we can try to compare our predictions with experiments done on Si whiskers and NW bending tests.

The measured fracture strength of Si whiskers with diameter at the micrometer scale ranges from 2 to 8 GPa. Eisner (1955) performed the tensile tests of $\langle 111 \rangle$ Si whiskers of $D < 1 \mu\text{m}$ and measured the strength of 3.8 GPa. Pearson et al. (1957) performed the bending test of $\langle 111 \rangle$ Si whiskers of $D \sim 20 \mu\text{m}$ and the fracture strength was measured up to 5 GPa at room temperature. Sandulva et al. (1964) also performed bending tests of Si whiskers of $D = 4 \mu\text{m}$ and found the fracture strength is 7.8 GPa at room temperature.

Tsuchiya et al. (2002) performed tensile tests of $\langle 110 \rangle$ oriented Si beams, which are 20 or 50 μm wide and 140 nm thick. The fracture strength up to 4.9 GPa was measured. Kizuka et al. (2005) performed tensile tests of $\langle 100 \rangle$ Si NW of $D = 6$ nm and reported the fracture strength of 5 GPa. However, their sample did not have a uniform cross-section and it fractures at the thinnest point where the NW contacts the substrate. This suggests

that the intrinsic strength of Si NW could be higher than 5 GPa. Hoffmann et al. (2006) measured an average fracture strength of 12 GPa from AFM bending tests of $\langle 111 \rangle$ -oriented Si NWs of $D = 90 \sim 190$ nm. Zhu et al. (2009) performed tensile experiments of Si NWs of $D = 15 \sim 60$ nm, and the fracture strength up to about 12.2 GPa was measured. The results of Hoffmann et al. (2006) and Zhu et al. (2009) are reasonably close to our MD simulations. The slightly higher value predicted by the MD simulations (13~15 GPa), compared with experiments (12 GPa), is probably caused by the higher strain rate in the simulations.

4.2. Comparison with *in situ* tensile experiment

Our MD simulations predict that the fracture mechanism of $[110]$ Si NWs depends not only on the temperature but also on their diameter. The dependence of the fracture behavior of Si on temperature has been known for a long time. Pearson et al. (1957) reported that Si whiskers start to flow plastically between 600°C and 650°C. Interestingly, our simulations show that the thinner NW is, the more “ductile” it becomes. In particular, NWs with diameters below 4 nm fail by shear flow regardless of temperature. In a recent *in situ* tensile experiment of $[110]$ Si NWs at room temperature by Han et al. (2007), ductile failure is reported for Si NWs with diameters $D < 60$ nm. This is to be compared with an earlier experiment on $\langle 111 \rangle$ Si NW with diameters in the range of 100 ~ 200 nm, where brittle failure without plastic deformation was reported (Heidelberg et al., 2006).

It is encouraging that the size effect on the fracture mechanisms of Si NWs predicted by our simulation is in qualitative agreement with the *in situ* experiment (Han et al., 2007). However, the critical diameter predicted by our simulations (4 nm) is much smaller than that observed experimentally (60 nm). There can be several reasons for this discrepancy.

First, due to the fundamental time scale limit of MD, the strain rate in our simulations, $\dot{\epsilon} = 5 \times 10^8 \text{ s}^{-1}$, is about 13 orders of magnitude higher than that in the experiment. Intuitively, a higher strain rate (and a lower temperature) would lead to a more brittle behavior, which is consistent with the difference observed here. Second, the (200 keV) electron beam in *in situ* experiments can enhance dislocation mobility (Maeda and Takeuchi, 1990; Levade et al., 1991; Werner et al., 1995; Vanderschaeve et al., 2000) and may also be responsible for the extensive amorphization observed under the applied load.

Some of our simulation data contradict the explanation offered by Han et al. (2007) for the observed size dependence of ductility. Han et al. (2007) attributed the enhanced ductility in thin NWs to a significant reduction of Young's modulus for NWs with $D < 60$ nm. However, our calculations and another study based on first-principles (Lee and Rudd, 2007) show that the Young's modulus of a NW does not change appreciably from the bulk value until the diameter is less than 6 nm. Even though our data do show a (slight) reduction of Young's modulus at $D \leq 3$ nm, we do not believe this effect is strong enough to explain the change of fracture mechanism observed in our simulations. In addition, recent tensile experiments by Zhu et al. (2009) have shown that brittle fracture of Si NWs with no plasticity even though significant reduction of Young's modulus is observed over the tested diameters between 15 and 60 nm. Unfortunately, the NW direction in this experiment is unknown and could be either $\langle 110 \rangle$, $\langle 111 \rangle$, or $\langle 112 \rangle$. We hope more tensile experiments of smaller NWs with controlled orientations will be performed in the near future so that our predictions of the size effect can be tested.

4.3. Dislocation nucleation versus dislocation mobility

To understand what controls the fracture behavior of NWs, it is useful to first review some of the models that have been proposed to explain the mechanism of the BDT of bulk single crystal silicon. Historically, two different models have been proposed: one based on dislocation nucleation (Rice and Thomson, 1974) and the other based on dislocation mobility (Samuels and Roberts, 1989; Hirsch et al., 1989; Hsia and Argon, 1994). Both models assume a crack pre-existing somewhere in the crystal.

In the nucleation-controlled model, the material is brittle if a dislocation cannot nucleate from the crack tip before the crack starts to propagate. However, experimental evidences (Burns and Webb, 1970; Samuels and Roberts, 1989) seem to support the mobility-controlled model. At temperatures slightly below the BDT temperature, dislocations can still nucleate at the crack tip, but they cannot move away fast enough. Ultimately the crack still propagates and the material remains brittle. This happens because the local stress field rapidly decreases as the dislocation moves away from the crack tip. The dislocation will stop moving if the local stress is much lower than the Peierls stress.

It is interesting to find out whether the brittle/ductile behavior of a Si NW is controlled by dislocation mobility or dislocation nucleation. In the fol-

lowing, we will present several arguments in favor of a nucleation-controlled model for Si NWs. First, the NWs in our simulations (as well as in many experiments) are free from pre-existing cracks. Hence both crack and dislocation need to be nucleated, preferably from the surface.³ Second, when failure occurs, the applied stress greatly exceeds the Peierls stress of the dislocation (see Section 3.3, due to the lack of a pre-existing crack). Hence the dislocation, once nucleated, is able to move across the entire cross section, even at very low temperature.

The latter idea is confirmed by a zero-temperature simulation, in which we introduce a straight screw dislocation one lattice spacing below the surface layer of a Si NW of $D = 7$ nm. Under the applied stress of $\sigma_{zz} = 13$ GPa, the dislocation moves completely across the NW on the slip plane during the energy minimization simulation, leaving a step on the NW surface. Based on these results, we believe that the NW fracture mechanism is determined by whether the first nucleation event is that of a dislocation or a crack. Further study is needed to quantify the nucleation energy barrier of a dislocation and a crack from the NW surface, and to explain why the nucleation barrier for a dislocation is lower than that for a crack when the NW becomes sufficiently thin.

5. Summary

Our MD simulations predict that the fracture mechanism of Si NWs depends not only on the temperature but also on the NW diameter, with thinner NWs exhibiting a shear failure mechanism regardless of temperature. Our prediction is qualitatively consistent with the *in-situ* experiment of Han et al. (2007). We found that the shear failure and the cleavage fracture are initiated by the nucleation of a dislocation and a crack from the NW surface, respectively. Our results suggest that the fracture behavior of Si NWs is controlled by competition between crack and dislocation nucleations from the NW surface, contrary to the dislocation mobility-controlled model for describing BDT in bulk Si. As such, the preference of the shear failure mechanism by thin NWs, even at low temperatures, must be caused by the low energy barrier for dislocation nucleation in thin NWs.

³There is experimental evidence that dislocations seem to be easily generated at free surfaces of silicon (Kirscht et al., 1978).

Acknowledgment

We appreciate the kind help from Dr. G. Wagner for implementing the MEAM potential model in LAMMPS and allowing us to use it. We would like to thank Prof. W. D. Nix, Prof. A. S. Argon and Prof. J. K. Hsia for helpful discussions. We also appreciate Prof. G. A. Galli and Dr. T. Vo for providing the atomistic coordinates of Si NW in their *ab initio* calculation for comparison. This work is supported by the NSF/CMMI Nano-Bio-Materials program grant CMS-0556032.

References

- Alerhand, O. L., Vanderbilt, D., Meade, R. D., Joannopoulos, J. D., Oct 1988. Spontaneous formation of stress domains on crystal surfaces. *Physical Review Letters* 61 (17), 1973–1976.
- Baskes, M. I., 1992. Modified embedded-atom potentials for cubic materials and impurities. *Phys. Rev. B* 46 (5), 2727–2742.
- Baskes, M. I., 1997. Determination of modified embedded atom method parameters for nickel. *Materials Chemistry and Physics* 50, 152–158.
- Baskes, M. I., 1999. Atomistic potentials for the molybdenum-silicon system. *Materials Science and Engineering A261*, 165–168.
- Baskes, M. I., Angelo, J. E., Bisson, C. L., 1994. Atomistic calculations of composite interfaces. *Modelling Simul. Mater. Sci. Eng.* 2, 505–518.
- Bazant, M. Z., Kaxiras, E., 1997. Environment-dependent interatomic potential for bulk silicon. *Physical Review B* 56 (14), 8542–8552.
- Bhaduri, S. B., Wang, F. F. Y., 1986. Fracture surface energy determination in 1 1 1 planes in silicon by the double torsion method. *Journal of Materials Science* 21, 2489–2492.
- Branício, P. S., Rino, J.-P., Dec 2000. Large deformation and amorphization of ni nanowires under uniaxial strain: A molecular dynamics study. *Phys. Rev. B* 62 (24), 16950–16955.
- Burns, S. J., Webb, W. W., April 1970. Fracture surface energies and dislocation processes during dynamical cleavage of LiF. ii. experiments. *Journal of Applied Physics* 41 (5), 2086–2095.

- Cai, W., Bulatov, V. V., Chang, J., Li, J., Yip, S., 2004. Dislocation core effects on mobility. In: Nabarro, F. R. N., Hirth, J. P. (Eds.), *Dislocations in Solids*. Elsevier, Ch. 64.
- Chan, C. K., Peng, H., Lui, G., McIlwrath, K., Zhang, X. F., Huggins, R. A., Cui, Y., 16 Dec 2007. High-performance lithium battery anodes using silicon nanowires. *Nature Nanotechnology* 3, 31 – 35.
- Chau, M., Englander, O., Lin, L., Aug 12-14 2003. Silicon nanowire-based nanoactuator. In: *Proceedings of the 3rd IEEE conference on nanotechnology*. Vol. 2. San Francisco, CA, pp. 879–880.
- Chueng, P. S. Y., 1977. On the calculation of specific heats, thermal pressure coefficients and compressibilities in molecular dynamics simulations. *Molecular Physics* 33, 519–526.
- Cormier, J., Rickman, J. M., Delph, T. J., 2001a. Erratum: Stress calculation in atomistic simulations of perfect and imperfect solids. *J. Appl. Phys.* 89 (7), 4198.
- Cormier, J., Rickman, J. M., Delph, T. J., 2001b. Stress calculation in atomistic simulations of perfect and imperfect solids. *J. Appl. Phys.* 89 (1), 99–104.
- Cui, Y., Lauhon, L. J., Gudixsen, M. S., Wang, J., Lieber, C. M., 9 Apr 2001a. Diameter-controlled synthesis of single-crystal silicon nanowires. *Applied Physics Letters* 78 (15), 2214–2216.
- Cui, Y., Wei, Q., Park, H., Lieber, C. M., 2001b. Nanowire nanosensors for highly sensitive and selective detection of biological and chemical species. *Science* 293, 1289–1292.
- Cui, Y., Zhong, Z., Wang, D., Wang, W. U., Lieber, C. M., 2003. High performance silicon nanowire field effect transistors. *Nano Letters* 3, 149–152.
- Dommelen, L. V., 2003. Physical interpretation of the virial stress.
URL <http://eng.fsu.edu/~dommelen/papers/virial/index.pdf>
- Eisner, R. L., 1955. Tensile tests on silicon whiskers. *Acta Metallurgica* 3, 414–415.

- Gall, K., Diao, J., Dunn, M. L., 2004. The strength of gold nanowires. *Nano Lett.* 4, 2431–2436.
- García, A., Northrup, J. E., Dec 1993. Stress relief from alternately buckled dimers in si(100). *Phys. Rev. B* 48 (23), 17350–17353.
- Gilman, J. J., 1960. Direct measurements of the surface energies of crystals. *Journal of Applied Physics* 31 (12), 2208–2218.
URL <http://link.aip.org/link/?JAP/31/2208/1>
- Hahm, J., Lieber, C. M., 2004. Direct ultrasensitive electrical detection of DNA and DNA sequence variations using nanowire nanosensors. *Nano Letters* 4 (1), 51–54.
- Han, X., Zheng, K., Zhang, Y., Zhang, X., Zhang, Z., Wang, Z. L., 2007. Low-temperature in situ large-strain plasticity of silicon nanowires. *Adv. Mater.* 19, 2112 – 2118.
- Hauch, J. A., Holland, D., Marder, M. P., Swinney, H. L., 1999. Dynamic fracture in single crystal silicon. *Phys. Rev. Lett.* 82, 3823–3826.
- Heidelberg, A., Ngo, L. T., Wu, B., Phillips, M. A., Sharma, S., Kamins, T. I., Sader, J. E., Boland, J. J., 2006. A generalized description of the elastic properties of nanowires. *Nano Letters* 6 (6), 1101–1106.
- Hirsch, P. B., Roberts, S. G., Samuels, J., 1989. The brittle-ductile transition in silicon. II. interpretation. *Proc. Roy. Soc. Lond. A* 421, 25–53.
- Hoffmann, S., Utke, I., Moser, B., Michler, J., Christiansen, S. H., Schmidt, V., Senz, S., Werner, P., Gösele, U., Ballif, C., 2006. Measured of the bending strength of vapor-liquid-solid grown silicon nanowires. *Nano Letters* 6 (4), 622–625.
- Holmes, J. D., Johnston, K., Doty, R. C., Korgel, B. A., 2000. Control of thickness and orientation of solution-grown silicon nanowires. *Science* 287, 1471.
- Hoover, W. G., 1985. Canonical dynamics: Equilibrium phase-space distributions. *Phys. Rev. A* 31, 1695–1697.

- Hsia, K. J., Argon, A. S., 1994. Experimental study of the mechanisms of brittle-to-ductile transition of cleavage fracture in Si single crystals. *Mater. Sci. Eng.* A176, 111–119.
- Huang, Y., Lieber, C. M., 2004. Integrated nanoscale electronics and optoelectronics: Exploring nanoscale science and technology through semiconductor nanowires. *Pure Appl. Chem.* 76, 2051–2068.
- Ikeda, H., Qi, Y., Çagin, T., Samwer, K., Johnson, W. L., Goddard, W. A., Apr 1999. Strain rate induced amorphization in metallic nanowires. *Phys. Rev. Lett.* 82 (14), 2900–2903.
- Jaccodine, R. J., 1963. Surface energy of germanium and silicon. *Journal of The Electrochemical Society* 110 (6), 524–527.
URL <http://link.aip.org/link/?JES/110/524/1>
- Kang, K., Cai, W., 2007. Brittle and ductile fracture of semiconductor nanowires – molecular dynamics simulations. *Philosophical Magazine* 87, 2169–2189.
- Kirscht, F. G., Doerschel, J., Hansch, C., 1978. Some observations concerning the initial state of plastic flow in silicon. *Phys. Stat. Sol. A* 47, K17.
- Kizuka, T., Takatani, Y., Asaka, K., Yoshizaki, R., 2005. Measurements of the atomistic mechanics of single crystalline silicon wires of nanometer width. *Phys. Rev. B* 72, 035333–1–6.
- Koizumi, H., Kamimura, Y., Suzuki, T., 2000. Core structure of a screw dislocation in a diamond-like structure. *Phil. Mag. A* 80, 609–620.
- Lee, B., Rudd, R. E., 2007. First-principles calculation of mechanical properties of Si $\langle 001 \rangle$ nanowires and comparison to nanomechanical theory. *Physical Review B* 75, 195328.
- Levade, C., Couderc, J. J., Vanderschaeve, G., Caillard, D., Couret, A., 1991. TEM *in-situ* observation of recombination-enhanced mobility of dislocations in II-VI compounds. *Applied Surface Science* 50, 119 – 124.
- Li, J., 2003. Atomeye: an efficient atomistic configuration viewer. *Modell. Simul. Mater. Sci. eng.* 11, 173–177.
URL <http://164.107.79.177/Archive/Graphics/A/>

- Li, X., Ono, T., Wang, Y., Esashi, M., 13 Oct 2003. Ultrathin single-crystalline-silicon cantilever resonators: Fabrication technology and significant specimen size effect on young's modulus. *Applied Physics Letters* 83 (15), 3081 – 3083.
- Liu, F., Lagally, M. G., Apr 1996. Interplay of stress, structure, and stoichiometry in ge-covered si(001). *Phys. Rev. Lett.* 76 (17), 3156–3159.
- Ma, D. D. D., Lee, C. S., Au, F. C. K., Tong, S. Y., Lee, S. T., 21 Mar 2003. Small-diameter silicon nanowire surfaces. *Science* 299.
- Maeda, N., Takeuchi, S., June 1990. Enhanced dislocation mobility by electron-beam irradiation in GaP. *Japanese Journal of Applied Physics* 29 (6), 1151 – 1152.
- Marc, G., McMillan, W. G., 1985. The virial theorem. In: Prigogine, I., Rice, S. A. (Eds.), *Advances in Chemical Physics*. Vol. 58. Interscience, pp. 209–361.
- Martyna, G. J., Tuckerman, M. E., Tobias, D. J., Klein, M. L., 1996. Explicit reversible integrators for extended systems dynamics. *Molecular Physics* 87 (5), 1117–1157.
- Meade, R. D., Vanderbilt, D., 1991. Microscopic origins of stress on semiconductor surfaces. In: Tong, S. Y., Hove, M. A. V., Takayanagi, K., Xie, X. D. (Eds.), *The structure of surfaces III*. Vol. 24 of Springer series in surface sciences. Springer-Verlag, pp. 4–8, proceedings of the 3rd International conference on the Structure of Surfaces (ICSOS III), Milwaukee, WI, U.S.A. July 9-12, 1990.
- Morales, A. M., Lieber, C. M., 9 Jan 1998. A laser ablation method for the synthesis of crystalline semiconductor nanowires. *Science* 279, 208–211.
- Nix, W. D., Gao, H., 1998. An atomistic interpretation of interface stress. *Scripta Materialia* 39 (12), 1653–1661.
- Nosé, S., 1984. A molecular dynamics method for simulations in the canonical ensemble. *Molecular Physics* 52, 255–268.
- Park, H. S., Gall, K., Zimmerman, J. A., Sep. 2006. Deformation of fcc nanowires by twinning and slip. *Journal of the Mechanics and Physics of Solids* 54 (9), 1862–1881.

- Park, H. S., Zimmerman, J. A., Mar. 2006. Stable nanobridge formation in $\langle 110 \rangle$ gold nanowires under tensile deformation. *Scripta Materialia* 54 (6), 1127–1132.
- Patolsky, F., Timko, B. P., Yu, G., Fang, Y., Greytak, A. B., Zheng, G., Lieber, C. M., 25 Aug 2006. Detection, simulation, and inhibition of neuron signals with high-density nanowire transistor arrays. *Science* 313, 1100–1104.
- Paulo, A. S., Bokor, J., Howe, R. T., He, R., Yang, P., Gao, D., Carraro, C., Maboudian, R., 2005. Mechanical elasticity of single and double clamped silicon nanobeams fabricated by the vapor-liquid-solid method. *Appl. Phys. Lett.* 87, 053111.
- Payne, M. C., Robers, N., Needs, R. J., Needels, M., Joannopoulos, J. D., 1989. Total energy and stress of metal and semiconductor surfaces. *Surface Science* 211/212, 1–20.
- Pearson, G. L., Jr., W. T. R., Feldmann, W. L., 1957. Deformation and fracture of small silicon crystals. *Acta Metallurgica* 5, 181–191.
- Pizzagalli, L., Beauchamp, P., Nov. 2004. First principles determination of the peierls stress of the shuffle screw dislocation in silicon. *Philosophical Magazine Letters* 84 (11), 729–736.
- Plimpton, S., 1995. Fast parallel algorithms for short-range molecular dynamics. *Journal of Computational Physics* 117, 1–19.
URL <http://lammps.sandia.gov/>
- Rice, J. R., Thomson, R., 1974. Ductile versus brittle behaviour of crystals. *Philos. Mag.* 29 (1), 73 – 97.
- Samuels, J., Roberts, S. G., 1989. The brittle-ductile transition in silicon. I. experiments. *Proc. Roy. Soc. Lond. A* 421, 1–23.
- Sandulva, A. V., Bogoyavlenskii, P. S., Dronyuk, M. I., 1964. Preparation and some properties of whisker and needle-shaped single crystals of germanium and silicon and their solid solutions. *Soviet Physics Solid State* 5 (9), 1883 – 1888.

- Stillinger, F. H., Weber, T. A., 1985. Computer simulation of local order in condensed phase of silicon. *Phys. Rev. B* 31, 5262–5271.
- Swadener, J. G., Baskes, M. I., Nastasi, M., 2002. Molecular dynamics simulation of brittle fracture in silicon. *Phys. Rev. Lett.* 89, 085503.
- Tersoff, J., 1989. Modeling solid-state chemistry: Interatomic potentials for multicomponent systems. *Phys. Rev. B* 39, 5566–5568.
- Tian, B., Zheng, X., Kempa, T. J., Fang, Y., Yu, N., Yu, G., Huang, J., Lieber, C. M., Oct. 18 2007. Coaxial silicon nanowires as solar cells and nanoelectronic power sources. *Nature* 449, 885–890.
- Tsuchiya, T., Shikida, M., Sato, K., 2002. Tensile testing system for sub-micrometer thick films. *Sensors and Actuators A* 97–98, 492–496.
- Vanderschaeve, G., Levade, C., Caillard, D., 2000. Transmission electron microscopy *in situ* investigation of dislocation mobility in semiconductors. *Journal of Physics: Condensed Matter* 12, 10093 – 10103.
- Vo, T., Williamson, A. J., Galli, G., 2006. First principles simulations of the structural and electronic properties of silicon nanowires. *Physical Review B* 74, 045116.
- Wang, D., Wang, Q., Javey, A., Tu, R., Dai, H., 2003. Germanium nanowire field-effect transistors with SiO_2 and high- κ HfO_2 . *Appl. Phys. Lett.* 83, 2432–2434.
- Werner, M., Weber, E. R., Bartsch, M., Messerschmidt, U., 1995. Carrier injection enhanced dislocation glide in silicon. *Physica Status Solidi (a)* 150, 337 – 341.
- Wu, B., Heidelberg, A., Boland, J. J., 2005. Mechanical properties of ultrahigh-strength gold nanowire. *Nature Mater.* 4, 525–529.
- Wu, Y., Cui, Y., Huynh, L., Barrelet, C. J., Bell, D. C., Lieber, C. M., 2004. Controlled growth and structures of molecular-scale silicon nanowires. *Nano Letters* 4 (3), 433–436.
- Zhu, Y., Xu, F., Qin, Q., Fung, W. Y., Lu, W., 19 Aug 2009. Mechanical properties of vapor-liquid-solid synthesized silicon nanowires. *Nano Letters* 9 (11), 3934 – 3939.

Zimmerman, J. A., Kelchner, C. L., Klein, P. A., Hamilton, J. C., Foiles, S. M., Oct 2001. Surface step effects on nanoindentation. Phys. Rev. Lett. 87 (16), 165507.

Table A.1: Parameters for the MEAM potential of Si, including the cut-off radius $r_c(\text{\AA})$, the cohesive energy $E_c(\text{eV})$, equilibrium nearest neighbor distance $r_e(\text{\AA})$, and other parameters defined in Baskes (1992). The value for $t^{(1)}$ corresponds to the use of Legendre polynomials (Baskes, 1999) (*i.e.* `legend = 0.6`).

	r_c	E_c	r_e	α	A	$\beta^{(0)}$	$\beta^{(1)}$	$\beta^{(2)}$	$\beta^{(3)}$	$t^{(1)}$	$t^{(2)}$	$t^{(3)}$	<code>cmin</code>	<code>cmax</code>
Si	6.0	4.63	2.35	4.87	1.0	4.4	5.5	5.5	5.5	2.05	4.47	-1.8	2.0	2.8

A. MEAM model and benchmarks

In order to test how accurately the MEAM model describes the atomistic structure on the NW surfaces, we compare a relaxed structure of NW of $D = 3$ nm with that from *ab initio* simulations (Vo et al., 2006) based on the density functional theory (DFT). The two relaxed structures are shown side by side in Fig. A.1, where only Si atoms are plotted, even though the Si NW surface is passivated with hydrogen atoms in the *ab initio* simulation.

Reconstruction on Si surfaces can usually be described by the formation of dimers, in which two surface atoms move toward each other to form a new bond. It is encouraging to observe similar pattern of dimer formation on NW surfaces using both MEAM and *ab initio* models. Dimers both parallel and perpendicular to the NW axis are observed and the location and orientation of the dimers are identical in both models. Quantitative comparisons on the surface dimer bond length are shown in Table A.2, which shows that the MEAM model predicts surface dimers reasonably well when compared with the *ab initio* model, while other potentials do not. This gives further justification for the use of the MEAM potential model when modelling the fracture behavior of Si NWs.

Surface energy and surface stress are also important properties to test because they can affect crack or dislocation nucleation from surface. In Kang and Cai (2007), we calculated the (1 1 0) surface opening energy as a function of the opening distance as two blocks are rigidly displaced. In the same manner, the unreconstructed surface energies of the (1 1 1) shuffle-set plane and the (1 0 0) plane are calculated here. The surface energies of three low index planes are compared with experimental values in Table A.3. Overall, the surface energies predicted by MEAM are close to the experimental values,

Table A.2: Surface dimer bond length. This table lists the bond length of surface dimers shown in Fig.A.1. The symbols \longleftrightarrow and \updownarrow refer the dimers along the NW direction and normal to the NW direction, respectively. The value in the parenthesis designate the ratio of the dimer bond length over the distance between the same atomic pair in the bulk. The latter is $5.431/\sqrt{2} = 3.84$ Å for MEAM potential and $5.39/\sqrt{2} = 3.81$ Å for DFT. For the purpose of comparison, the last two columns show the interatomic distances between the atomic pairs for structure relaxed by EDIP (Bazant and Kaxiras, 1997) and Tersoff (Tersoff, 1989) potentials. Relaxation using EDIP and Tersoff potentials barely shows any surface reconstruction.

Surface Dimer	MEAM		DFT		EDIP	Tersoff
\longleftrightarrow	2.49 Å	(65 %)	2.39 Å	(63 %)	3.87 Å	3.88 Å
\updownarrow	2.48 Å	(65 %)	2.38 Å	(63 %)	3.78 Å	3.74 Å

Table A.3: Surface energy (meV/Å²) of low index crystal planes. The surface energies obtained from MEAM Si (Baskes, 1992) are close to the experimental values (Gilman, 1960; Jaccodine, 1963; Bhaduri and Wang, 1986).

	(111)	(110)	(100)
MEAM Si	78.3	95.9	116
Exp.	71.1~77.4	113~119	133 ^a

^aThe (100) surface energy is estimated by Jaccodine (1963) from the measured (111) surface energy.

Table A.4: Surface stress (meV/Å²) on the (2 × 1) reconstructed (001) surface. σ_{\parallel} is the surface component along the dimer bond direction, and σ_{\perp} is the surface component perpendicular to the dimer bond. The results are compared with TB or DFT calculations.

	σ_{\parallel}	σ_{\perp}
Alerhand et al. (1988)	35	-35
Payne et al. (1989)	47	-132
Meade and Vanderbilt (1991)	106	-60
Liu and Lagally (1996)	73	-129
García and Northrup (1993)	130	-27
MEAM Si	45	-59

and the trend of the energy reduction in the order of (1 0 0), (1 1 0), and (1 1 1) is correctly captured.

In order to check how accurately surface stress is captured by MEAM, we calculate the surface stress on a (2 × 1) reconstructed (001) plane, because we observe dimer formations on the (001) facet of a Si NW in Fig. A.1. Surface stress σ_{ij} is defined in the Lagrangian coordinates as

$$\sigma_{ij}^L = \frac{\partial \gamma_0}{\partial \epsilon_{ij}^L}, \quad (\text{A.1})$$

where ϵ_{ij}^L is the strain defined in the embedded coordinate system and γ_0 is the energy per unit reference area (Nix and Gao, 1998). For atomistic calculations in a simulation cell containing two free surfaces, Eq. (A.1) can be written as

$$\sigma_{ij} = \frac{1}{2A_0} \frac{\partial (E_1(\epsilon_{ij}) - E_0(\epsilon_{ij}))}{\partial \epsilon_{ij}}, \quad (\text{A.2})$$

where $2A_0$ is the area of the free surfaces at reference state, and $E_0(\epsilon_{ij})$ and $E_1(\epsilon_{ij})$ are the potential energies of relaxed structures of a perfect bulk crystal and a crystal of same size with free surfaces, respectively, at a given strain ϵ_{ij} .

The surface stress from the MEAM potential is listed in Table A.4 and compared with the results from tight binding (TB) and DFT calculations. The MEAM prediction of surface stress is within the range of those obtained from other calculations. Furthermore, the MEAM potential correctly captures the feature that the sign of the surface stress depends on the direction.

We have also computed the Peierls stress of the shuffle-set screw dislocation in Si by the MEAM potential. The dislocation is introduced in a supercell with periodic vectors $4[1\ 1\ \bar{2}]$, $10[1\ 1\ 1]$, and $2[1\ \bar{1}\ 0]$ along x , y , and

z directions, respectively. Periodic boundary conditions are applied in the x and z directions, but free surfaces are created in the y -direction. Shear stress is applied to the top and bottom layers of surface atoms in increments of 1 MPa, followed by conjugate gradient relaxation, until the dislocation moves. The Peierls stress predicted by the MEAM is found to be 2.23 GPa. This is consistent with the prediction from the SW potential (2 GPa) (Koizumi et al., 2000; Cai et al., 2004), but lower than a DFT prediction (4 GPa) (Pizzagalli and Beauchamp, 2004).

List of Figures

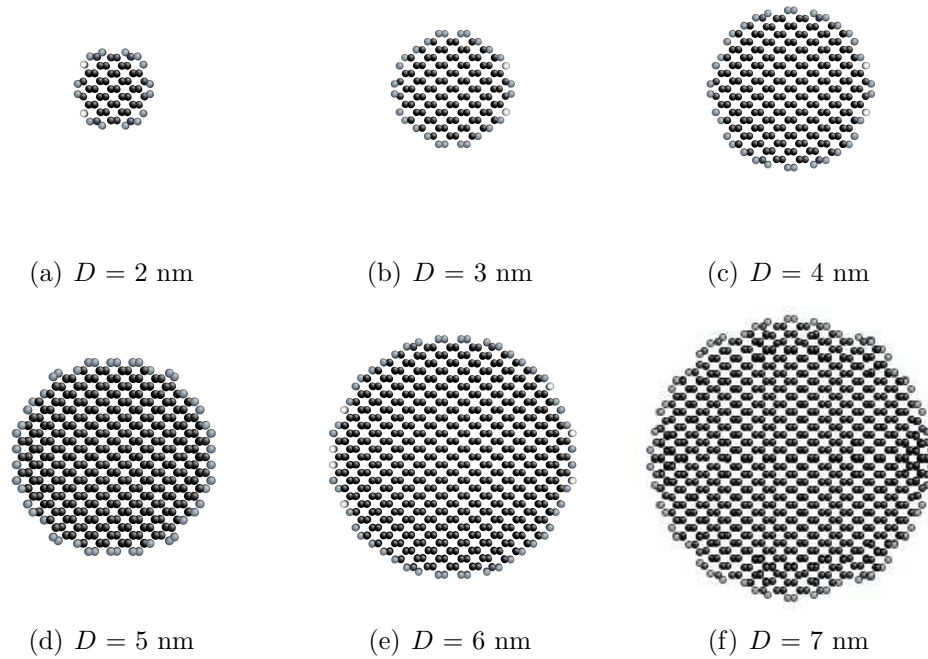


Figure 1: Cross sections of $[110]$ -oriented Si NWs after relaxation. Atoms are colored by their local energy. Surface atoms have higher energy than interior atoms. The atomic structures are visualized by Atomeye (Li, 2003).

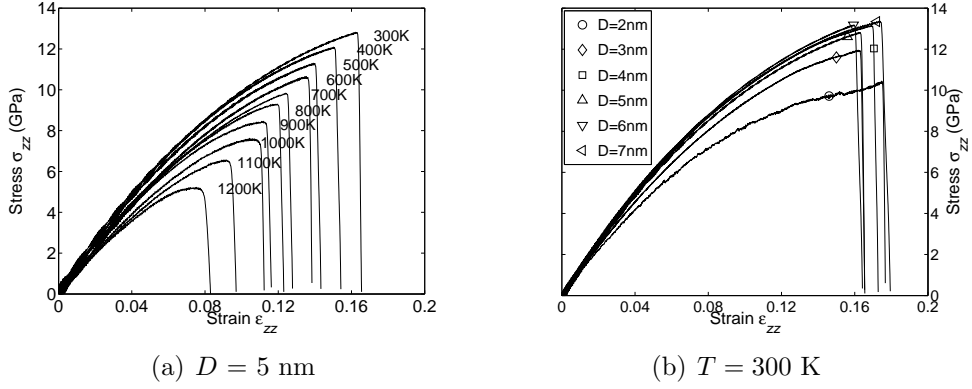


Figure 2: (a) Tensile stress-strain curves of Si NW with diameter $D = 5 \text{ nm}$ at different temperatures. (b) Tensile stress-strain curves of Si NW with different diameters at $T = 300 \text{ K}$.

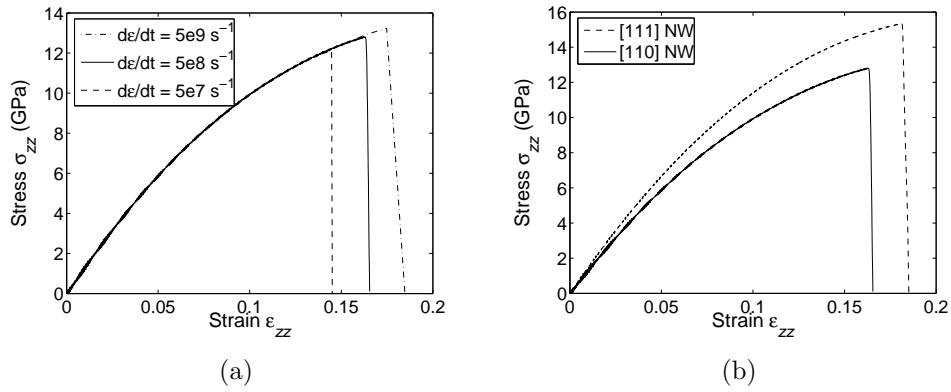
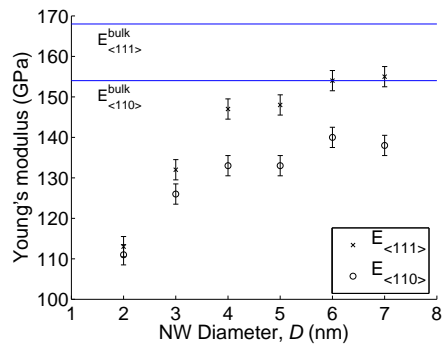
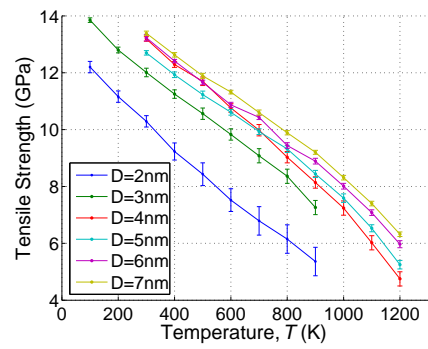


Figure 3: (a) Tensile stress-strain curves of [110]-oriented Si NW of $D = 5 \text{ nm}$ at $T = 300 \text{ K}$ loaded at different strain rates. (b) Tensile stress-strain curves of [111] and [110] Si NWs of $D = 5 \text{ nm}$ at $T = 300 \text{ K}$.



(a)



(b)

Figure 4: (a) Young's modulus of Si NWs as a function of diameter D at $T = 300$ K. (b) Tensile strength of Si NW as a function of temperature for NWs with different diameters.

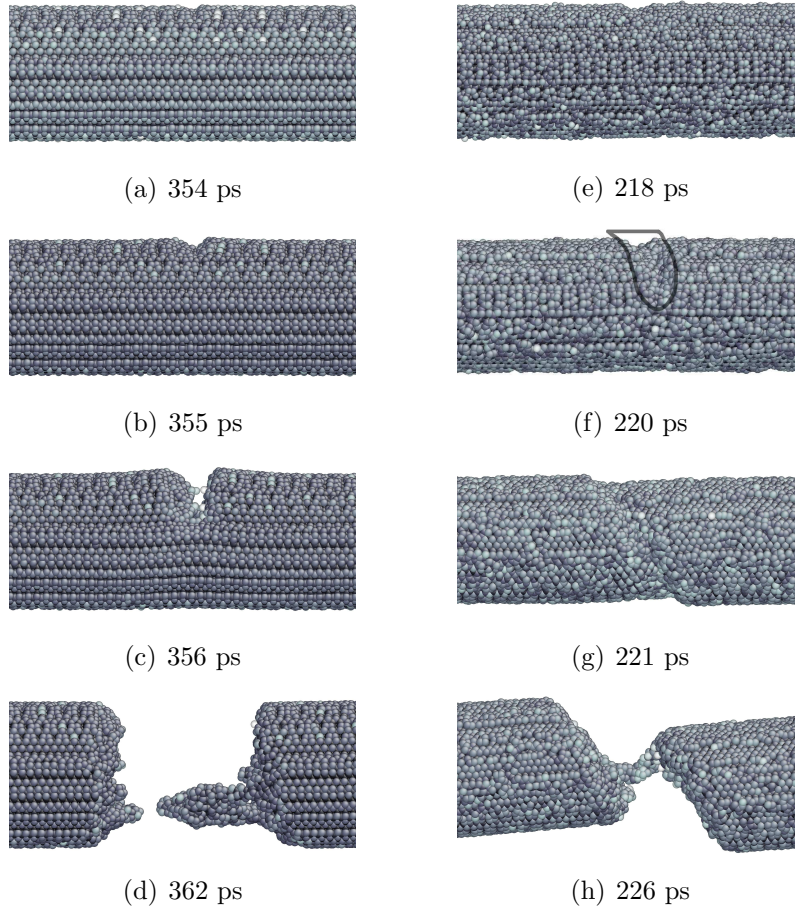


Figure 5: Snapshots of a $[110]$ Si NW with $D = 7$ nm during fracture under tensile loading: (a-d) $T = 300$ K; (e-h) $T = 1000$ K. The numbers below each figure are the time elapsed since the beginning of tensile loading. In (d), the atomic fragment attached to the right section of the fractured NW is only limited to the surface layer. The lines in (f) highlights the surface area that undergoes local slip.

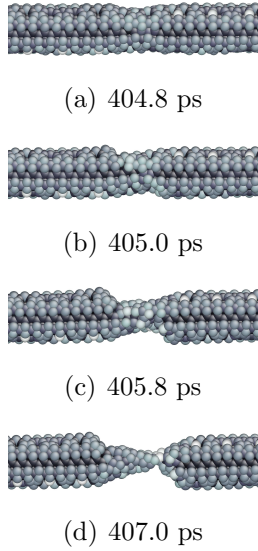


Figure 6: Snapshots of a $[110]$ Si NW with $D = 2$ nm during ductile fracture at $T = 100$ K. The numbers below each figure are the time elapsed since the beginning of tensile loading.

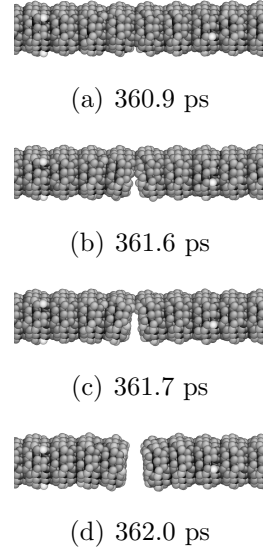
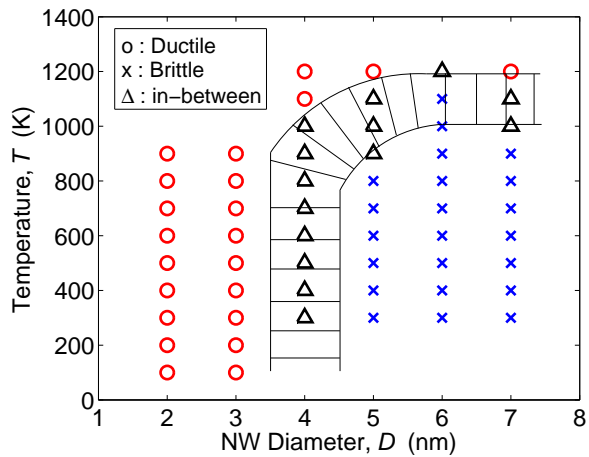


Figure 7: Snapshots of a $[111]$ Si NW with $D = 2$ nm during brittle fracture at $T = 300$ K. The numbers below each figure are the time elapsed since the beginning of tensile loading.

Figure 8: Ductile-brittle domain map with NW diameter as the x -axis and temperature as the y -axis. Each symbol corresponds to ten independently repeated simulations with random initial velocities. A symbol \circ designates ductile fracture and a symbol \times does brittle fracture. For Δ symbols, out of ten simulations a Si NW can fail in a brittle or ductile manner or sometimes in a mixture of both.



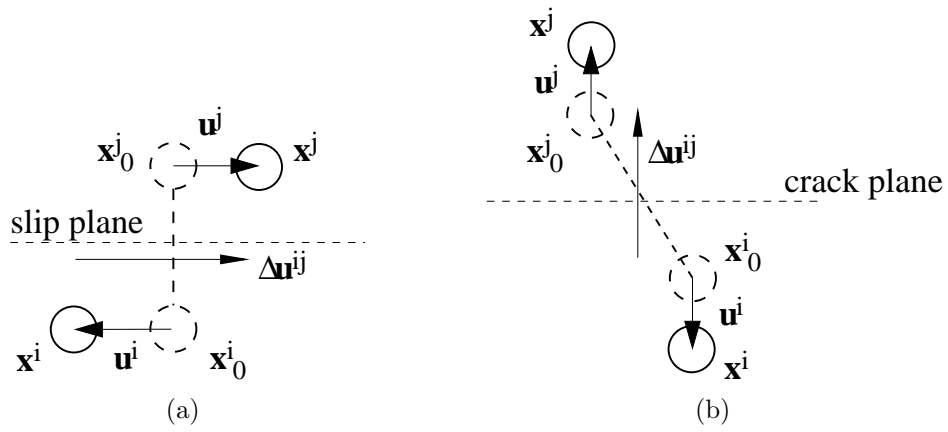


Figure 9: A bond that connects a pair of atoms i and j in the reference configuration $\{\mathbf{x}_0^i\}$, is drawn in a dashed line. The atoms i and j are displaced by \mathbf{u}^i and \mathbf{u}^j , respectively, in the configuration $\{\mathbf{x}^i\}$. The displacement difference vector $\Delta\mathbf{u}^{ij} \equiv \mathbf{u}^j - \mathbf{u}^i$ can indicate (a) slip if the slip plane cuts the bond between atoms i and j , or (b) bond breaking by crack.

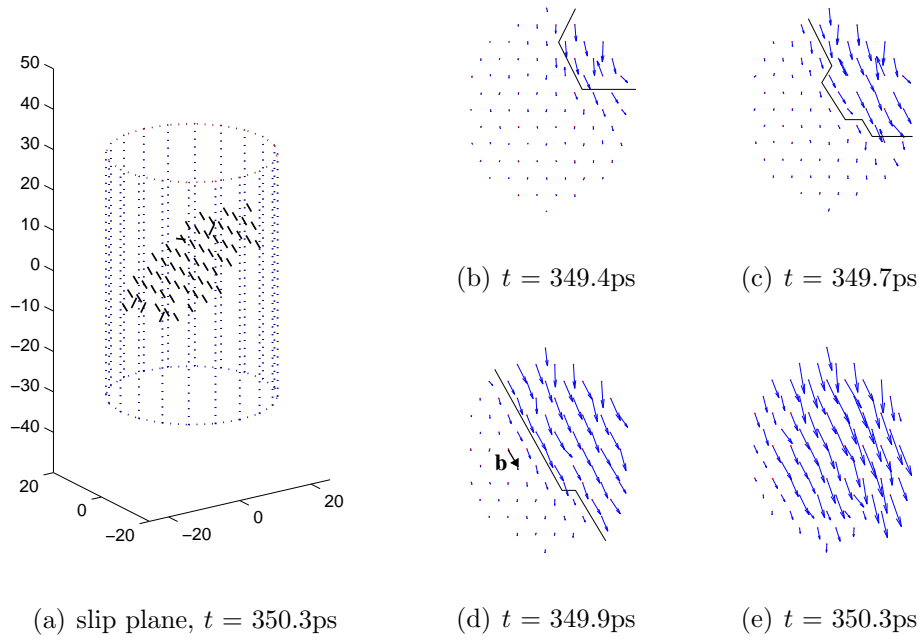


Figure 10: Si NW of $D = 4\text{nm}$ at $T = 300\text{K}$. (a) A slip plane is visualized by showing the atomic bonds across which the atomic displacement difference is greater than 3.84 \AA . (b)-(e) Displacement difference vectors $\Delta\mathbf{u}^{ij}$ across the bonds identified in (a) are shown at different time steps. Dots are used to notify the center of atomic bonds in the reference structure. (d) The black bold arrow is the Burgers vector $\mathbf{b} = [011]/2$ on the slip plane $(11\bar{1})$. The lines in (b), (c), and (d) are drawn to guide the eye.

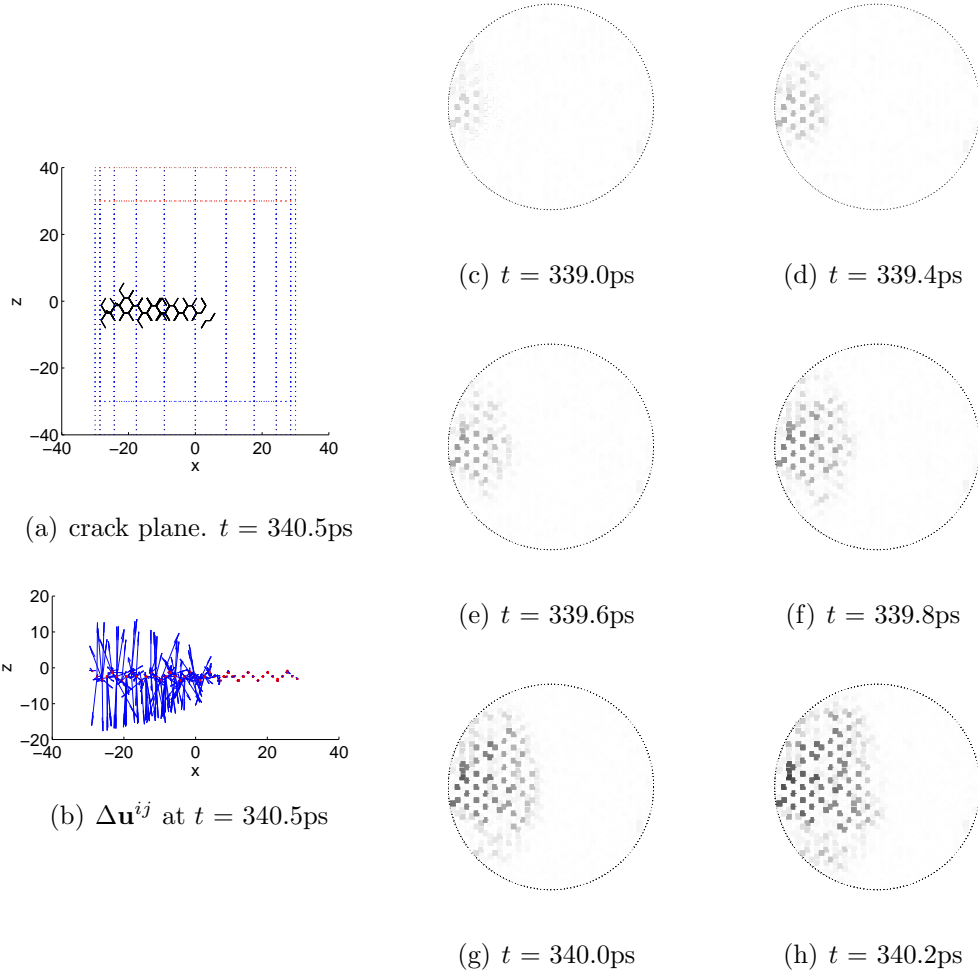


Figure 11: Si NW of $D = 6$ nm at $T = 300$ K. (a) A crack plane is visualized by showing the atomic bonds across which the atomic displacement difference is greater than 3.84 Å. (b) The displacement difference vector $\Delta \mathbf{u}^{ij}$ located at the bond center. (c)–(h) The z component of $\Delta \mathbf{u}^{ij}$ vectors are shown in gray scale.

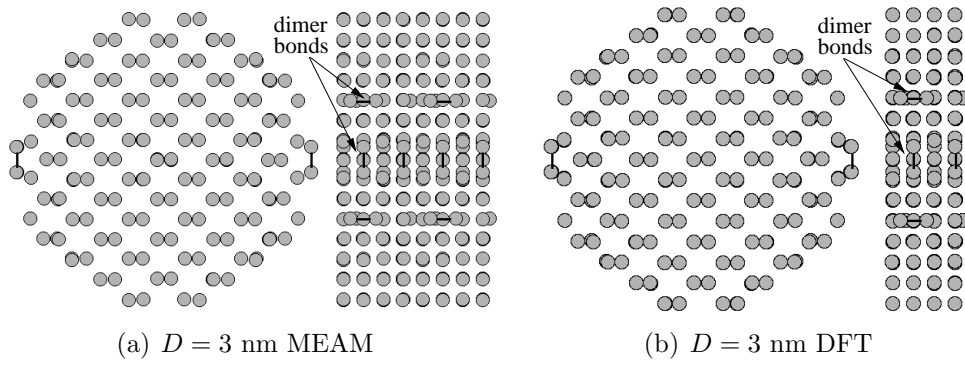


Figure A.1: Comparing the relaxed atomistic structure of Si NWs using (a) the MEAM model and (b) the *ab initio* DFT model for diameters $D = 3$ nm. Surface dimer bonds are drawn when the interatomic distance is less than 2.5 \AA .